7

Tomography

In this chapter we consider systems that provide important "tomographic" or three-dimensional capability. The tomogram is effectively an image of a slice taken through a three-dimensional volume. Ideally, it is free of the effects of intervening structures, thus providing a distinct improvement in the ability to visualize structures of interest.

In single-projection radiography the resultant image is the superposition of all the planes normal to the direction of propagation. In essence the system has infinite depth of focus, although, as was shown in Chapter 4, the finite source size causes planes closer to the recorder to have better resolution. Ignoring this effect and assuming parallel rays, the recorded image is given by

$$I_d(x, y) = I_0 \exp\left[-\int \mu(x, y, z)dz\right]. \tag{7.1}$$

This integration over z often prevents a suitable diagnosis of the characteristics of a section at a given depth plane. Since all other planes are superimposed, the subtle contrast variations of the desired plane are often obscured. This is particularly true in studies of lung lesions where the superimposed rib structures obscure the visualization.

MOTION TOMOGRAPHY

Until very recently the only method of isolating a view of a single plane was motion tomography [Meredith and Massey, 1977], as shown in Fig. 7.1. The source and the recorder are moved in opposite directions. As shown, one plane in the object remains in focus while all others have their images blurred. The nature and degree of the deblurring is determined by the distance of each plane from the focused plane and by the extent and type of motion of the source and film. These systems are often classified by the type of motion undertaken, such as linear, circular, and hypercycloidal tomography. The mechanisms that accomplish these motions are quite elaborate since they must be both accurate and rapid, so that the motions can be completed in a few-second breath-holding interval.

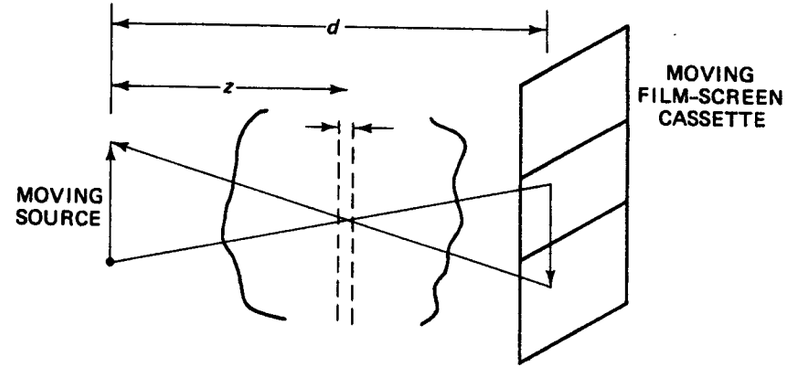

FIG. 7.1 Motion tomography.

In general, the source undergoes a specific motion in a plane parallel to the recorder plane. The path as a function of time can be characterized as $g(x, y, t)$. The path, in general, is a two-dimensional delta line function which defines the motion of the source. From this motion and the corresponding motion of the film, we can calculate the resultant impulse response.

Using the source motion of $g(x, y, t)$, we immediately see that the resultant path on a stationary film using a pinhole transparency is $g(x/m, y/m, t)$ by straightforward geometry. Thus the path due to source motion experiences the same magnification, $m = -(d - z)/z$, as did the source image in Chapter 4. As indicated, to provide a tomographic plane, the film is moved in a scaled version of the source motion. Whenever the source is displaced from the axis at a point (x, y), the film center is positioned at $-kx$, $-ky$, where k is a positive number representing the scaling of the film motion. Thus the center of the film traverses a path $g(x/-k, y/-k, t)$.

As the film moves, the resultant path of a beam on the film moves in the opposite direction with respect to film coordinates. Thus the resultant path

incident on the film due to the two motions is the impulse response, which is given by

$$h(x_d, y_d, t) = Bg\left(\frac{x_d}{k+m}, \frac{y_d}{k+m}, t\right) \tag{7.2}$$

where $(k + m)$ is the total magnification due to both motions and B is a normalizing constant that will be subsequently evaluated. The integrated impulse response is therefore

$$\begin{aligned} h(x_d, y_d) &= B \int g\left(\frac{x_d}{(k+m)}, \frac{x_y}{(k+m)}, t\right) d(vt) \\ &= Bf\left(\frac{x_d}{k+m}, \frac{y_d}{k+m}\right) \end{aligned} \tag{7.3}$$

where $f(x, y)$ is the integrated path traversed by the source as given by

$$f(x, y) = \int g(x, y, t) d(vt) \tag{7.4}$$

where v is the source velocity in the direction of motion. The resultant recorded path, as given above, is

$$f\left(\frac{x_d}{k+m}, \frac{y_d}{k+m}\right).$$

This impulse response, because of the geometry, is independent of the lateral coordinates of the object and can thus be placed in convolutional form for each depth plane z. The resultant image due to a transparency t at plane z is given by

$$\begin{aligned} I_d(x_d, y_d) &= t ** h \\ &= t\left(\frac{x_d}{M}, \frac{y_d}{M}\right) ** Bf\left(\frac{x_d}{k+m}, \frac{y_d}{k+m}\right). \end{aligned} \tag{7.5}$$

In evaluating the normalizing constant B, we use similar reasoning to that employed in Chapter 4. We assume that the total number of photons used during the exposure is N. If the source is translated uniformly, the number of photons emitted per unit distance during the exposure is N/L, where L is the line integral of the path $f(x, y)$ as given by

$$L = \iint f(x, y) dx dy. \tag{7.6}$$

Although this is a two-dimensional integration, it represents a line integral since $f(x, y)$ is a delta line function. Thus the constant B, representing the intensity per unit distance at the detector plane, is given by

$$B = \frac{KN}{L4\pi d^2(k+m)^2} \cos^3 \theta = \frac{I_i}{L(k+m)^2} \tag{7.7}$$

where I_i is the incident intensity as defined in (4.2), (4.4), and (4.5), and K is proportional to the energy per photon. Ignoring obliquity factors we can set $I_i = I_0$, the intensity at the axis, which assumes that $\cos^3 \theta \simeq 1$. The resultant detected intensity becomes

$$I_d(x_d, y_d) = t\left(\frac{x_d}{M}, \frac{y_d}{M}\right) ** \frac{I_0}{L(k+m)^2} f\left(\frac{x_d}{k+m}, \frac{y_d}{k+m}\right). \tag{7.8}$$

The most widely used form of motion tomography is linear tomography, where the source and film are both moved uniformly in straight lines in opposite directions. The source motion is described by

$$g(x, y, t) = \delta(x - vt)\delta(y) \operatorname{rect}\left(\frac{vt}{X}\right) \tag{7.9}$$

where v is the velocity of the source in the x direction and X is the extent of the traverse. The resultant source path is given by

$$f(x, y) = \int g(x, y, t) d(vt) = \operatorname{rect}\left(\frac{x}{X}\right)\delta(y) \tag{7.10}$$

indicating a line of length X in the x direction. The resultant detected image from (7.8) becomes

$$I_d(x_d, y_d) = t\left(\frac{x_d}{M}, \frac{y_d}{M}\right) ** \frac{I_0}{X(k+m)} \operatorname{rect}\left[\frac{x_d}{X(k+m)}\right]\delta(y_d). \tag{7.11}$$

The $\delta(y_d)$ in the expression above could be eliminated by defining the convolution as being one-dimensional in the x direction only. Thus each point at plane z is smeared into a horizontal line of length $X(k + m)$. At the desired plane z_0 we have

$$k = -m = \frac{d - z_0}{z_0} \tag{7.12}$$

where the rect function becomes a narrow delta function and reproduces the transparency in its original form. The plane of interest is at the depth $z_0 = d/(k + 1)$. A chest tomogram using linear motion is shown in Fig. 7.2. Note the defocusing of the ribs and spine.

In the frequency domain the Fourier transform of t is multiplied by the Fourier transform of the point-spread function h. For the case shown above, we have

$$I_d(u, v) = I_0 M^2 T(Mu, Mv) \operatorname{sinc}[X(k + m)u]. \tag{7.13}$$

Thus, in the u direction, a plane at z is multiplied by a low-pass filter having an effective bandwidth of approximately $[X(k + m)]^{-1}$. At the desired plane $z = z_0$, this becomes an infinite-bandwidth filter and does not affect the frequency response $I_d(u, v)$. All other planes experience various degrees of filtering.

When using a finite source rather than a point source, the total impulse response is the convolution of the motion path function and source size as given by

$$h(x_d, y_d) = \frac{1}{4\pi d^2 m^2} s\left(\frac{x_d}{m}, \frac{y_d}{m}\right) ** \frac{1}{L(k+m)^2} f\left(\frac{x_d}{k+m}, \frac{y_d}{k+m}\right). \tag{7.14}$$

Thus at the tomographic plane $z = z_0$ where $m = -k$ and f becomes a delta function, the resolution continues to be limited by the source size. The expression in (7.14) reduces to that of the point source as given by (7.5) and (7.7) if we substitute $s(x, y) = KN\delta(x, y)$.

FIG. 7.2 Chest tomograph, using linear motion of source of detector.

Circular Motion

As was indicated, many other motions can be used other than the linear motion described. The linear motion has the disadvantage that planes other than the desired tomographic plane experience blurring in one dimension only. Thus edges parallel to the x axis receive no blurring at all. Structures of this type in any plane will remain sharply defined and can interfere with the visualization of structures in the desired plane. The alternative is the use of two-dimensional motions such as circles, hypercycloids, and so on. A circular motion can be described using the polar coordinate equivalent of the delta function where

$$\delta(x - x_0, y - y_0) = \frac{\delta(r - r_0)}{r}\delta(\theta - \theta_0). \tag{7.15}$$

The circular motion is described by

$$g(x, y, t) = g(r, \theta, t) = \frac{\delta(r - r_0)}{r}\delta(\theta - \omega t)\,\text{rect}\left(\frac{\omega t}{2\pi}\right) \tag{7.16}$$

representing a single circular traverse. The resultant source path is described as

$$f(x, y) = \int \frac{\delta(r - r_0)}{r}\delta(\theta - \omega t)\,\text{rect}\left(\frac{\omega t}{2\pi}\right)rd(\omega t)$$

$$= \delta(r - r_0)\,\text{rect}\left(\frac{\theta}{2\pi}\right) = \delta(r - r_0). \tag{7.17}$$

The film center also moves in a circle at the opposite side of the axis having a radius kr_0. When the source is at r_0, θ_0 the film center is at $kr_0, \theta_0 + \pi$. The resultant impulse response from (7.3) and (7.7) is given by

$$h(x_d, y_d) = h(r) = \frac{I_0}{2\pi r_0(k + m)}\delta[r - (k + m)r_0]. \tag{7.18}$$

Motion tomography has two basic disadvantages. First, for each tomographic plane, the entire volume of interest is exposed by x-rays. If a number of sections are desired, as is usually the case, the radiation can be extensive. Second, in motion tomography, the detail contrast in the plane of interest is not improved over a conventional radiograph. All planes other than the plane of interest are blurred or smeared out, leaving the desired plane as the only one with any detailed structure. Thus the sharp details of the interfering structures in other planes are removed, which significantly improves the visualization even though the detail contrast in the desired plane is unchanged.

Multiple-Radiograph Tomography; Tomosynthesis

The second of the disadvantages, the detail contrast being the same as that of conventional radiography, is fundamental to motion tomography. The first of the disadvantages, however, can be remedied by a system shown in Fig. 7.3 known as *tomosynthesis* [Grant, 1972], where the desired plane is selected after the x-ray procedure. Here a sequence of different radiographs are taken with the source in different positions and the subject and film in the same posi-

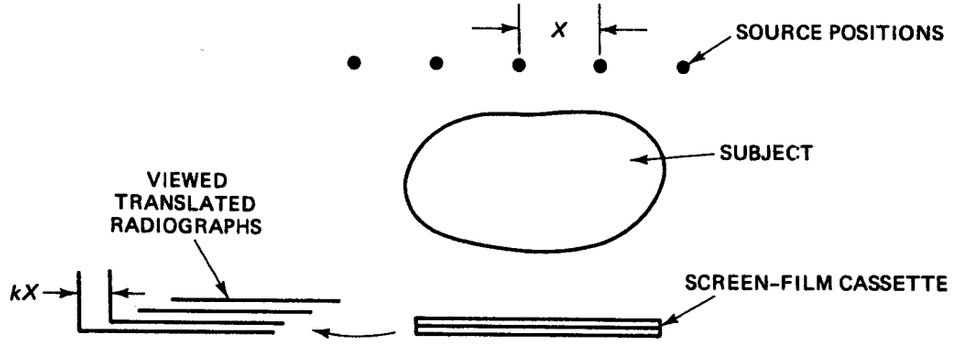

FIG. 7.3 Sequence of radiographs used to create a tomogram.

tion. The resultant films are stacked together and translated with respect to each other to select the desired plane. Assuming that the resultant composite image is the sum of the individual detected images, the path function $f(x, y)$ is a sum of point-source positions given by

$$f(x, y) = \delta(y) \sum_{i=-n/2}^{n/2} \delta(x - iX) \tag{7.19}$$

where n is the number of source positions and X is the separation between source positions. The value of k, representing the translation of the individual radiographs, is determined after the x-ray exposures are made, where each transparency is separated from its neighbor by kX. The resultant effective detected intensity for a given plane $t(x, y)$ using (7.8) is given by

$$I_d(x_d, y_d) = t\left(\frac{x_d}{M}, \frac{y_d}{M}\right) ** \delta(y_d) \frac{1}{n} \sum_{i=-n/2}^{n/2} \delta[x_d - i(k + m)X]. \tag{7.20}$$

The line integral L becomes n, the sum of the source positions, and the $(k + m)^2$ normalization in the denominator is canceled by the factors in the delta functions. It is clear that k is readily chosen to select the desired plane of interest. Since each film is given approximately $1/n$ of the exposure normally required, the system requires no increase in radiation dose for the ability to select planes after the exposure. The system requires a relatively rapid film changer so that the n exposures can be accomplished in a breath-holding interval of a few seconds. The out-of-focus planes are smeared by a series of points that approach a line. Using an appropriate mechanical structure the separation of the radiographs can be continuously varied with the plane of focus continuously moving through the object. Alternatively, the information can be collected and stored electronically, using television fluoroscopy, with the translation and summation taking place in a computer.

CODED SOURCE TOMOGRAPHY

Another approach to tomography is the use of a relatively large complex source $s(x, y)$. The recorded image, as studied in Chapter 4, is given by

$$s\left(\frac{x}{m}, \frac{y}{m}\right) ** t\left(\frac{x}{M}, \frac{y}{M}\right).$$

This recording can be considered the encoded image I_e. This encoded image is not useful of itself because of the complex source function.

The desired image, at any plane of interest, is decoded by cross correlation with $s(x/m_1, y/m_1)$, the source function at a particular plane z_1 where $m_1 = -(d - z_1)/z_1$. The decoded image is given by

$$I_d = I_e \star\star s\left(\frac{x}{m_1}, \frac{y}{m_1}\right)$$

$$= \left[s\left(\frac{x}{m_1}, \frac{y}{m_1}\right) \star\star s\left(\frac{x}{m}, \frac{y}{m}\right)\right] ** t\left(\frac{x}{M}, \frac{y}{M}\right). \tag{7.21}$$

The source function $s(x, y)$ is chosen to have a sharp autocorrelation peak, approaching a two-dimensional delta function. Thus at $z = z_1$, I_d will faithfully reproduce the plane $t(x/M_1, y/M_1)$ where $M_1 = d/z_1$. For $z \neq z_1$, the cross-correlation function will become broad, thus blurring all other planes. Some representative functions for $s(x, y)$ are a random array of points or a Fresnel zone plate. The considerations are similar to those of coded apertures in Chapter 8.

The decoding can be accomplished in a digital computer. For a given encoded image $I_e(x, y)$, any desired plane can be chosen by using the appropriate cross-correlation function $s(x/m_1, y/m_1)$. The basic difficulty with this system is that $s(x, y)$ is fundamentally a nonnegative function. It thus has limited capability for providing the desired autocorrelation peak. At best, the autocorrelation will have a peak riding on a large plateau. This plateau effectively represents an integration over a large portion of the image. This can distort the low-frequency response and result in poor noise performance. As a result, this approach has not been used commercially.

COMPUTERIZED TOMOGRAPHY

Motion tomography, at best, represents a limited ability to isolate a specific plane. In general the contrast of the plane of interest is unchanged over that of a projection radiograph. If a lesion in the plane results in a 1% difference in recorded intensity in a conventional radiograph, it will continue to be 1% different in the motion tomogram. The out-of-focus planes, however, will be blurred.

In 1973 a revolutionary concept in tomography, known as *computerized axial tomography*, was introduced by EMI Ltd. of England. This system provides an isolated image of a section within a volume completely eliminating all other planes [Herman, 1980; Gordon, 1975; Ledley, 1976; Scudder, 1978; Brooks and DiChiro, 1976a; Cho, 1974]. Thus the contrast of the image is not diminished by intervening structures. Thus far, computerized tomography has been extremely successful in clinical use. Lesions and organs that were heretofore impossible to visualize are seen with remarkable clarity.

The basic system is shown in Fig. 7.4. An x-ray source is collimated into a narrow beam and scanned through the plane of interest. The transmitted

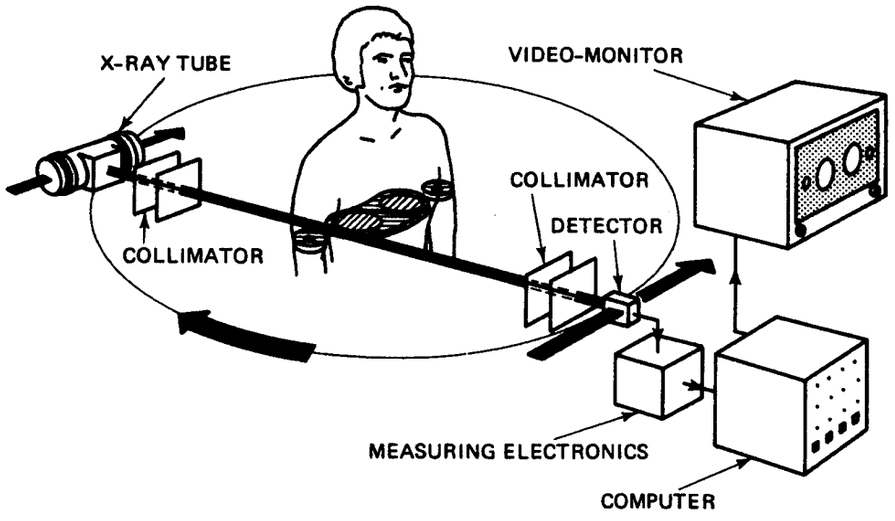

FIG. 7.4 Basic scanning system for computerized tomography. (Courtesy of the Siemens AG-Bereich Medizinische Technik.)

photons are detected by a scanning detector at each position of the scan. This same procedure is repeated at approximately 1° intervals for 180° so that a set of projections are obtained at approximately all angles. The resultant projection data are applied to a digital computer where an accurate two-dimensional image is reconstructed, representing the linear attenuation coefficient in the section of interest. The mathematics involved in the image reconstruction from projection data will be described.

This approach overcomes essentially all of the shortcomings of motion tomography. Only the section of interest is irradiated. Using carefully calibrated detectors, and limited only by the Poisson statistics of the number of counts per measurement, this technique has provided almost uncanny visualization of structures that were previously invisible. Radiologists have been able to perceive lesions whose attenuation coefficient differed by less than 0.5% from the surrounding tissue. Thus, in a noninvasive fashion, an accurate diagnosis is obtained.

RECONSTRUCTION MATHEMATICS—ITERATIVE APPROACHES

The mathematics involved is a relatively old, but seldom used, field of study involving the reconstruction of a two-dimensional distribution from its projections. The most straightforward, although computationally inefficient solution involves linear algebra. The two-dimensional image is reconstructed using a

matrix inversion of the projection data. For images of reasonable complexity, this is quite formidable. One general class of solutions involves an iterative procedure. This is an attempt to find a two-dimensional distribution that matches all of the projections. An initial distribution is assumed and it is compared with the measured projections. Using one of a variety of iterative algorithms, the initial distribution is successively modified. This method is known as the *Algebraic Reconstruction Technique*, or ART [Herman, 1980; Brooks and DiChiro, 1976a].

The ART system, illustrated in Fig. 7.5, is based on the very general premise that the resultant reconstruction should match the measured projections. The iterative process is started with all reconstruction elements f_i set to a constant such as the mean $\bar{f}$ or zero. In each iteration the difference between

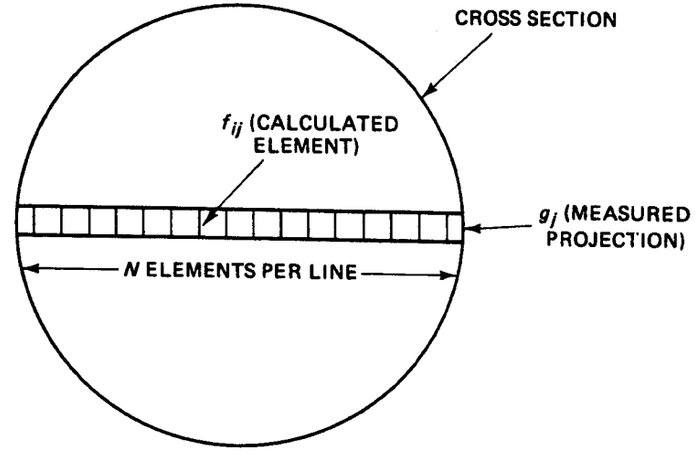

FIG. 7.5 ART system.

the measured data for a projection g_j and the sum of the reconstructed elements along that ray $\sum_{i=1}^{N} f_{ij}$ is calculated. Here f_{ij} represents an element along the jth line forming the projection ray g_j. This difference is then evenly divided among the N reconstruction elements. The iterative algorithm is defined as

$$f_{ij}^{q+1} = f_{ij}^{q} + \frac{g_j - \sum_{i=1}^{N} f_{ij}^{q}}{N} \tag{7.22}$$

where the superscript q indicates the iteration. The algorithm recursively relates the values of the elements to those of the previous iteration.

As an illustration of the ART process we use a simple 2 × 2 matrix of values and the associated measured projections.

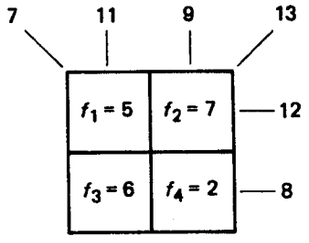

All six projection measurements, including the two verticals, two horizontals, and two diagonals, have been made. Presumably, these projection measurements are all that is available and, from these, the matrix of elements shown must be reconstructed. We begin the process arbitrarily by setting all values to zero, calculating the resultant projections, and comparing them to the measured projections. The differences are calculated, divided by the two elements per line, and added to each element.

Vertical rays:

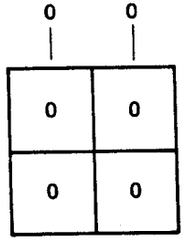

$$f_1^1 = f_3^1 = 0 + \frac{11 - 0}{2} = 5.5; \qquad f_2^1 = f_4^1 = 0 + \frac{9 - 0}{2} = 4.5$$

Horizontal rays:

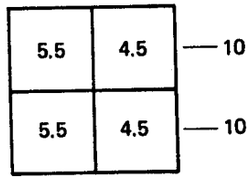

$$f_1^2 = 5.5 + \frac{12 - 10}{2} = 6.5; \qquad f_2^2 = 4.5 + \frac{12 - 10}{2} = 5.5$$

$$f_3^2 = 5.5 + \frac{8 - 10}{2} = 4.5; \qquad f_4^2 = 4.5 + \frac{8 - 10}{2} = 3.5$$

Diagonal rays:

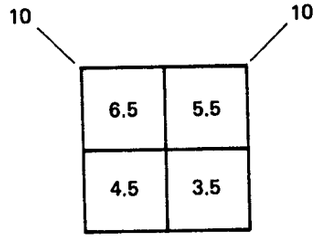

$$f_1^3 = 6.5 + \frac{7 - 10}{2} = 5; \qquad f_2^3 = 5.5 + \frac{13 - 10}{2} = 7$$

$$f_3^3 = 4.5 + \frac{13 - 10}{2} = 6; \qquad f_4^3 = 3.5 + \frac{7 - 10}{2} = 2$$

Thus the original elements are reconstructed. In general, for larger formats, many iterations, using the same measurement data over and over, are required for adequate convergence. The process is usually halted when the difference between the measured and calculated projections is adequately small.

A number of variations on this general theme have been proposed. One nonlinear formulation makes use of the known nonnegativity of the density values f_{ij}. Thus where $f_{ij} < 0$, it is set equal to zero. Another variation is known as *multiplicative ART*, as compared to the previous original algorithm, which is *additive ART*. In the multiplicative version the original density values are multiplied by the ratio of the measured line integral g_j to the calculated sum of the reconstructed elements. This is given by

$$f_{ij}^{q+1} = \frac{g_j}{\sum_{i=1}^{N} f_{ij}^q} f_{ij}^q. \tag{7.23}$$

In multiplicative ART, each reconstructed element is changed in proportion to its magnitude. This is in sharp contrast to additive ART, where each element in the ray is changed a fixed amount, independent of its magnitude.

Although the iterative methods were the most popular in the earlier days of computerized tomography, they have become almost completely supplanted by direct methods due to problems such as computation time and convergence accuracy in the presence of noise. The direct methods provide a linear reconstruction formulation between a two-dimensional distribution and its projections.

DIRECT RECONSTRUCTION METHODS—FOURIER TRANSFORM APPROACH

Direct reconstruction methods are based on the central section theorem, which is illustrated with the aid of Fig. 7.6. As shown, a single projection is taken in the x direction, for convenience, forming a projection $g(y)$ given by

$$g(y) = \int f(x, y)dx. \tag{7.24}$$

This projection represents an array of line integrals in the x direction. For demonstrating the central section theorem we use the two-dimensional Fourier

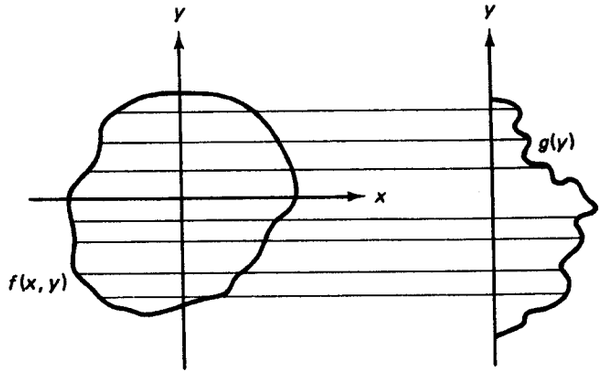

FIG. 7.6 Illustration of the central section theorem.

transform of the distribution $f(x, y)$ as given by

$$F(u, v) = \iint f(x, y) \exp\left[-i2\pi(ux + vy)\right]dxdy. \tag{7.25}$$

Along the $u = 0$ line this transform becomes

$$\begin{aligned} F(0, v) &= \iint f(x, y) \exp\left(-i2\pi v y\right)dxdy \\ &= \int\left[\int f(x, y)dx\right]e^{-i2\pi vy}dy \\ &= \mathfrak{F}_1\{g(y)\} \end{aligned} \tag{7.26}$$

where $\mathfrak{F}_1\{\cdot\}$ represents a one-dimensional Fourier transform. Thus, as shown in Fig. 7.7, the dashed $u = 0$ line in $F(u, v)$ is given by the Fourier transform

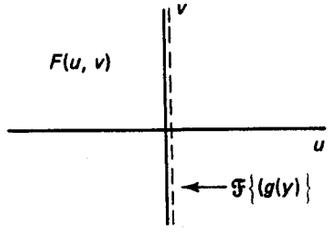

FIG. 7.7 Fourier domain illustration of the central section theorem.

of the projection of $f(x, y)$ in the x direction. Since the transform of each projection forms a radial line in $F(u, v)$, we can fill $F(u, v)$ by taking projections at many angles and taking their transforms. Once filled $F(u, v)$ is inverse transformed to reconstruct the desired density $f(x, y)$. This process can be studied in more detail using Fig. 7.8. Using a two-dimensional distribution $f(x, y)$, an array of line integrals are measured, each being a distance R from the origin

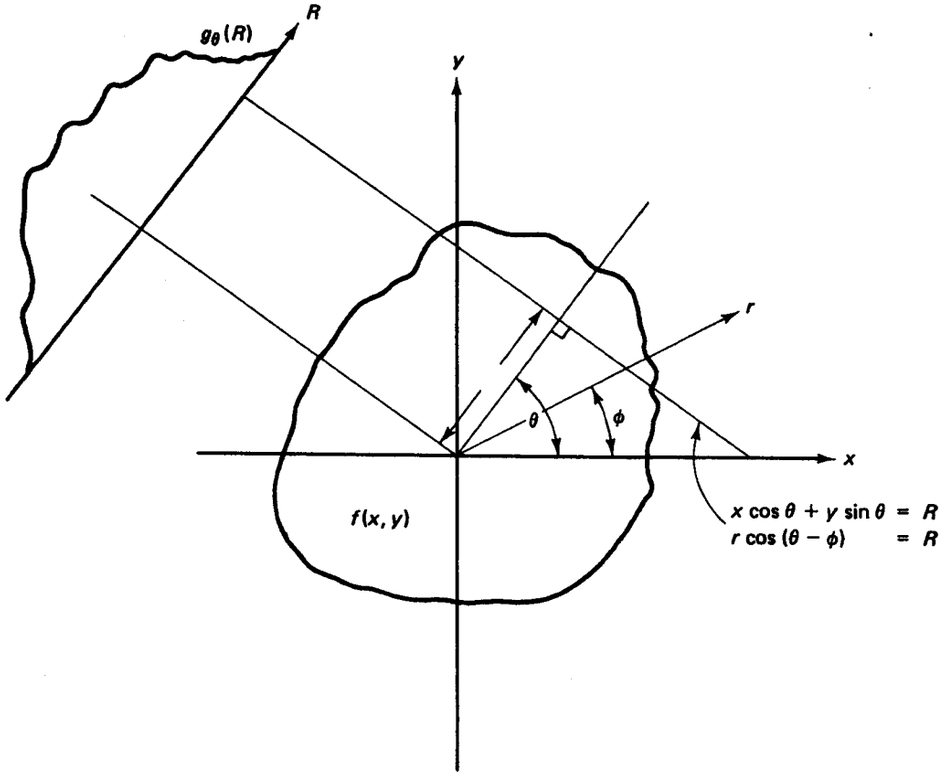

FIG. 7.8 Projection of a two-dimensional function.

where the perpendicular to the line is at an angle θ. This forms a projection given by

$$\begin{aligned} g_\theta(R) &= \iint f(x, y)\delta(x \cos\theta + y \sin\theta - R)dxdy \\ &= \int_0^{2\pi}\int_0^{\infty} f(r, \phi)\delta[r \cos(\theta - \phi) - R]rdrd\phi \end{aligned} \tag{7.27}$$

where $g_\theta(R)$ is the projection information in the θ direction. The integration takes place along line $x \cos\theta + y \sin\theta = R$ or, in polar coordinates r, ϕ, $r \cos(\theta - \phi) = R$. The delta line $\delta(x \cos\theta + y \sin\theta - R)$ sifts out the desired line in $f(x, y)$ to provide an effective line integration. The symbol $g_\theta(R)$ could alternatively have been written $g(R, \theta)$ since it is a two-dimensional function of the various projection angles θ and the distances R along each projection. However, the symbol $g_\theta(R)$ indicates a series of one-dimensional measurements at different distances R taken at a particular angle θ.

To provide a general derivation, the Fourier transform of the two-dimensional function $f(x, y)$ is given by

$$F(u, v) = \iint f(x, y)e^{-i2\pi(ux+vy)}dxdy. \tag{7.28}$$

Expressing this in polar coordinates $F(u, v) = F(\rho, \beta)$, where $u = \rho \cos \beta$ and $v = \rho \sin \beta$ gives

$$F(\rho, \beta) = \int\int f(x, y) e^{-i2\pi\rho(x \cos \beta + y \sin \beta)} dx dy. \tag{7.29}$$

The general central section theorem is shown by again mainpulating the two-dimensional Fourier transform to include the projection expression as given by

$$F(\rho, \beta) = \int\int\int f(x, y)\delta(x \cos \beta + y \sin \beta - R) \exp(-i2\pi\rho R) dx dy dR. \tag{7.30}$$

This expression clearly reduces to the basic Fourier transform relationship of equation (7.28) by integrating over R. By isolating the expression for the projection from equation (7.27), the Fourier transform of the image $f(x, y)$ can be rewritten as

$$F(\rho, \beta) = \int g_\beta(R) \exp(-i2\pi\rho R) dR \tag{7.31}$$

Therefore,

$$F(\rho, \beta) = \mathfrak{F}_1\{g_\beta(R)\}.$$

Thus the Fourier transform of a projection at angle β, as defined in Fig. 7.8, forms a line in the two-dimensional Fourier plane at this same angle. Since the projection angle θ and the resultant polar angle in the Fourier transform plane β are identical, we can use the same symbol θ for both. The transform of a projection in the transform plane, $F(\rho, \theta)$, is shown in Fig. 7.9. After filling the entire $F(\rho, \theta)$ plane with the transforms of the projections at all angles, the reconstructed density is provided by the two-dimensional inverse transform as

$$\begin{aligned} f(x, y) &= \int\int F(u, v) \exp[i2\pi(ux + vy)] du dv \\ &= \int_0^{2\pi} d\theta \int_0^{\infty} F(\rho, \theta) \exp[i2\pi\rho(x \cos \theta + y \sin \theta)] \rho d\rho. \end{aligned} \tag{7.32}$$

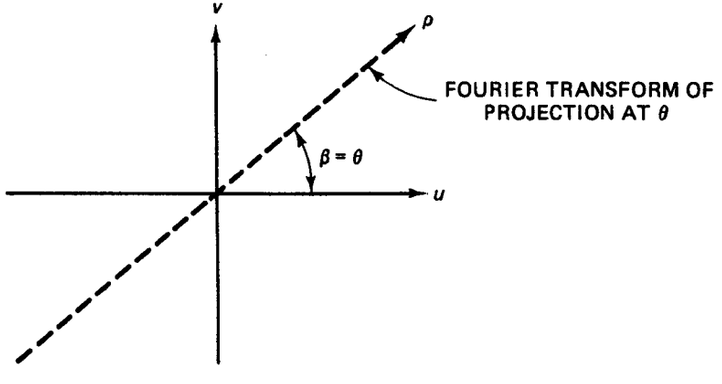

FIG. 7.9 Two-dimensional Fourier transform plane of distribution.

Figure 7.10 provides some physical insight into the central section theorem. In the top figure is a projection of a two-dimensional distribution $f(x, y)$. Using Fourier transform techniques $f(x, y)$ can be decomposed into an array of two-dimensional sinusoids. Two of the sinusoids are illustrated. In the center figure a projection is taken of a two-dimensional sinusoid. Since each ray experiences

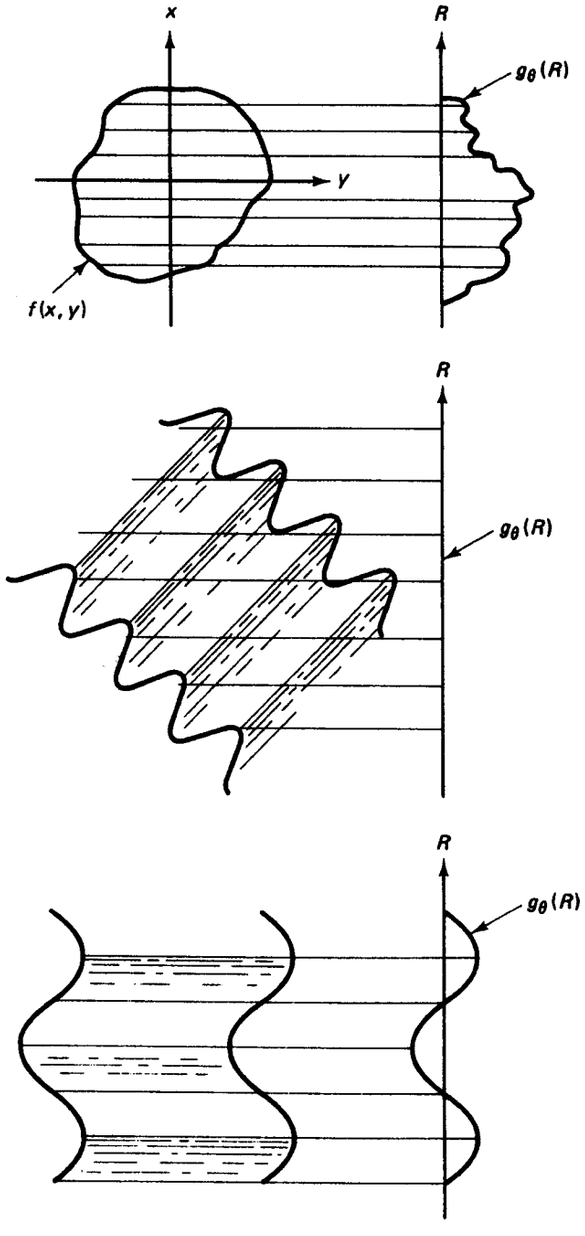

FIG. 7.10 Projections of sinusoidal components of a two-dimensional distribution.

equal positive and negative contributions, the resultant projection is zero. In the bottom figure the sinusoid is parallel to the projection angle. As a result, the projection is a one-dimensional sinusoid. Thus each projection extracts only those sinusoidal components at the projection angle. These components represent a line, as in Fig. 7.9, in Fourier space representing sinusoids of different frequencies at a specific angle.

EXAMPLES USING FOURIER TRANSFORM APPROACH

As an illustrative example we will consider two circularly symmetric cases of simple geometries. Circularly symmetric examples are being used solely for simplicity since the method is clearly applicable to any geometry. In the first example the measured projections at all angles are given by

$$g_\theta(R) = 2 \operatorname{sinc} 2R. \tag{7.33}$$

The two-dimensional Fourier transform at each angle θ is given by

$$F_\theta(\rho) = \mathfrak{F}\{g_\theta(R)\} = \operatorname{rect}\left(\frac{\rho}{2}\right), \tag{7.34}$$

where ρ, in this equation, is a one-dimensional variable along the θ direction. Adding up the contributions at all angles is equivalent to rotating the rect function over 180° to provide a symmetric two-dimensional frequency function

$$F(\rho, \theta) = F(\rho) = \operatorname{circ} \rho, \tag{7.35}$$

where the circ function is a "pillbox" with unity radius and unity height as defined in Chapter 2. The reconstructed density is the inverse transform of this function as given by

$$f(x, y) = f(r) = \mathfrak{F}^{-1}\{\operatorname{circ} \rho\} = \frac{J_1(2\pi r)}{r}. \tag{7.36}$$

This "jinc" function, named for its similarity to the sinc function, has a similar shape to the sinc function except that its zeros do not occur periodically and the amplitude of the ripples fall off more rapidly. Thus the projection of $J_1(2\pi r)/r$ is 2 sinc $2R$, a result that is certainly not intuitively obvious.

For the second example of circularly symmetric objects we use a cosinusoidal projection

$$g_\theta(R) = \cos \pi R. \tag{7.37}$$

As before, on each line in the transform, such as the u axis, we obtain

$$F(u) = \tfrac{1}{2}[\delta(u - \tfrac{1}{2}) + \delta(u + \tfrac{1}{2})].$$

Summing this pair of delta functions over 180°, we obtain

$$F(\rho) = \tfrac{1}{2}\delta(\rho - \tfrac{1}{2}) \tag{7.38}$$

representing a cylindrical shell in the frequency domain. The density is again given by the inverse transform. Using the Fourier–Bessel transform yields

$$f(r) = 2\pi \int_0^\infty F(\rho)\rho J_0(2\pi r\rho)d\rho = \frac{\pi}{2} J_0(\pi r). \tag{7.39}$$

Again we reach the unanticipated result that the projection of a $J_0(\cdot)$ function, the zeroth-order Bessel function of the first kind, is a cosine function.

ALTERNATIVE DIRECT RECONSTRUCTION—BACK PROJECTION

The computational problem with the central section theorem method shown is that a two-dimensional inverse transform is required. For computerized tomography this involves various interpolations and coordinate transformations. We now consider alternative reconstruction systems based on the same general principles but having distinct computational advantages. To do this we first introduce the concept of back projection [Gordon, 1975].

In back projection the measurements obtained at each projection are projected back along the same line, assigning the measured value at each point in the line. Thus the measured values are "smeared" across the unknown density function as if a line of wet ink, containing the measured projection values, is drawn across the reconstructed density function. This is shown in Fig. 7.11 for the case of an object consisting of a single point on the origin. Each projection is identical. Intuitively, we know, from each individual projection measurement, that a point of density lies somewhere along the line of

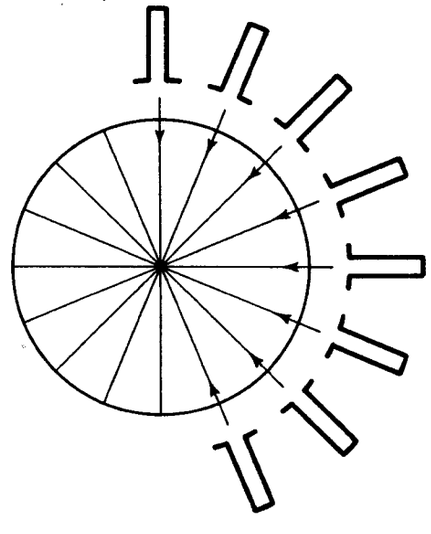

FIG. 7.11 Projections of a point at the origin back projected.

integration. It is thus reasonable, as an initial attempt at reconstruction, to assign the measured value along the entire line. We are essentially stating that we know that the point of density is somewhere along the line so that a "crude" reconstruction will result if we assign the measured value along the entire line.

Mathematically, the back projection of a single measured projection along the unknown density is given by

$$b_\theta(x, y) = \int g_\theta(R)\delta(x \cos\theta + y \sin\theta - R)dR \tag{7.40}$$

where $b_\theta(x, y)$ is the back-projected density due to the projection $g_\theta(R)$ at angle θ. Adding up these densities at all angles, we obtain

$$\begin{aligned} f_b(x, y) &= \int_0^\pi b_\theta(x, y)d\theta \\ &= \int_0^\pi d\theta \int_{-\infty}^{\infty} g_\theta(R)\delta(x \cos\theta + y \sin\theta - R)dR \end{aligned} \tag{7.41}$$

where $f_b(x, y)$ is the crude reconstruction resulting from pure back projection. This reconstruction is often called a *laminogram*. We will study the nature of the distortion in this reconstruction and attempt to correct it.

Using (7.27) and (7.41), we find the impulse response using back projection. We first find the projections $g_\theta(R)$ due to a delta function at the origin $\delta(r)/\pi r$ as given by

$$\begin{aligned} g_\theta(R) &= \int_0^{2\pi} \int_0^{\infty} \frac{\delta(r)}{\pi r}\delta[r \cos(\theta - \phi) - R]r dr d\phi \\ &= \int_0^{\pi} \int_{-\infty}^{\infty} \frac{\delta(r)}{\pi}\delta[r \cos(\theta - \phi) - R]dr d\phi \\ &= \int_0^{\pi} \frac{\delta(R)}{\pi} d\phi = \delta(R). \end{aligned} \tag{7.42}$$

Thus, as expected intuitively, each projection of a delta function at the origin is $\delta(R)$. These delta functions are back-projected giving the impulse response $h_b(r)$:

$$\begin{aligned} h_b(r) &= \int_0^\pi d\theta \int_{-\infty}^{\pi} \delta(R)\delta[r \cos(\theta - \phi) - R]\, dR \\ &= \int_0^\pi \delta[r \cos(\theta - \phi)]d\phi \\ &= \int_0^\pi \frac{\delta\left[\theta - \left(\frac{\pi}{2} + \phi\right)\right]}{\left|\frac{\partial}{\partial\theta} r \cos(\theta - \phi)\right|} d\theta \quad \text{evaluated at } \theta = \frac{\pi}{2} + \phi \\ &= \frac{1}{r} \end{aligned} \tag{7.43}$$

where we have made use of the delta function relationship [Bracewell,1965]

$$\delta[f(x)] = \sum \frac{\delta(x - x_n)}{|f'(x_n)|} \tag{7.44}$$

where x_n are the roots of $f(x)$.

Knowing the impulse response to be $1/r$, we write the reconstructed image from back projection

$$f_b(x, y) = f(x, y) ** \frac{1}{r}. \tag{7.45}$$

This represents a poor reconstruction in the case of reasonably complex images because of the "tails" of the $1/r$ response. Some early reconstructions were obtained of medical images using pure back projection with marginal results.

The $1/r$ blurring must be removed to provide the desired reconstruction. One approach makes use of the frequency-domain representation of (7.45), where

$$F_b(\rho, \theta) = \frac{F(\rho, \theta)}{\rho} \tag{7.46}$$

since the two-dimensional Fourier transform of $1/r$ is $1/\rho$. An obvious correction method is to take the Fourier transform of $f_b(x, y)$, weight the resultant $F_b(\rho, \theta)$ with ρ, and then inverse transform to provide the desired $f(x, y)$. This, however, has clearly not solved the computational problem since two two-dimensional transforms are required.

FILTERED BACK-PROJECTION RECONSTRUCTION SYSTEM

It is desirable to be able to use the elegant simplicty of back projection and to undo the $1/r$ blur without requiring two-dimensional transforms. This is accomplished by again making use of the powerful central section theorem.

We begin by restating the back-projection relationship for the laminogram $f_b(x, y)$ as

$$f_b(x, y) = \int_0^\pi d\theta \int_{-\infty}^{\pi} g(R, \theta)\delta(x \cos\theta + y \sin\theta - R)dR \tag{7.47}$$

and restructuring it into a Fourier transform mode by using the central section theorem to substitute the inverse transform of $F(\rho, \theta)$ for $g(R, \theta)$ as given by

$$f_b(x, y) = \int_0^\pi d\theta \int_{-\infty}^{\infty} \left[\int_{-\infty}^{\infty} F(\rho, \theta)e^{i2\pi\rho R}d\rho\right]\delta(x \cos\theta + y \sin\theta - R)dR. \tag{7.48}$$

Performing the integration over R, we obtain

$$f_b(x, y) = \int_0^\pi d\theta \int_{-\infty}^{\infty} F(\rho, \theta) \exp[i2\pi\rho(x \cos\theta + y \sin\theta)]d\rho. \tag{7.49}$$

To appreciate the significance of this relationship we restate the two-dimensional inverse Fourier transform relationship in polar form as

$$f(x, y) = \int_0^{2\pi} d\theta \int_0^{\infty} F(\rho, \theta) \exp [i2\pi\rho(x \cos \theta + y \sin \theta)]\rho d\rho. \quad (7.50)$$

We modify this equation to conform with (7.49), where the θ integration is from 0 to π and the ρ integration from $-\infty$ to ∞ as given by

$$f(x, y) = \int_0^{\pi} d\theta \int_{-\infty}^{\infty} F(\rho, \theta) \exp [i2\pi\rho(x \cos \theta + y \sin \theta)]|\rho| d\rho. \quad (7.51)$$

This form is equivalent to that of (7.50), where the integrand is Hermitian. This is clearly the case for physical systems where $f(x, y)$ is real and $F(\rho, \theta) = F(-\rho, \theta + \pi)$. It is necessary to use $|\rho|$ rather than ρ in (7.51) since the integration includes negative values.

Comparing (7.51) to the equation for the back-projected laminogram (7.49), we see that they differ only by the $|\rho|$ weighting as previously indicated. Substituting $\mathfrak{F}_1\{g_\theta(R)\}$ for $F(\rho, \theta)$ in (7.49), and dividing and multiplying by $|\rho|$, we obtain

$$f_b(x, y) = \int_0^{\pi} d\theta \int_{-\infty}^{\infty} \frac{\mathfrak{F}_1\{g_\theta(R)\}}{|\rho|} \exp [i2\pi\rho(x \cos \theta + y \sin \theta)]|\rho| d\rho. \quad (7.52a)$$

This equation provides an alternative interpretation to back projection. In essence, the transform of each projection $g_\theta(R)$ has been weighted by $1/|\rho|$ along each radial line in Fig. 7.9. This accounts for the blurred reconstruction of $f_b(x, y)$. This can therefore be removed by weighting each transformed projection with $|\rho|$ prior to back projection to create an undistorted reconstruction as given by

$$f(x, y) = \int_0^{\pi} d\theta \int_{-\infty}^{\infty} \frac{\mathfrak{F}_1\{g_\theta(R)\} \cdot |\rho|}{|\rho|} \exp [i2\pi\rho(x \cos \theta + y \sin \theta)]|\rho| d\rho. \quad (7.52b)$$

When we operate on each projection $g_\theta(R)$ the radial frequency variable ρ assumes the role of a one-dimensional frequency variable.

This reconstruction approach is known as the filtered back projection system. It is widely used since it involves only one-dimensional transforms. Each projection is individually transformed, weighted with the one-dimensional variable $|\rho|$, inverse transformed, and back projected. This is seen by rewriting (7.52) as

$$f(x, y) = \int_0^{\pi} d\theta \int_{-\infty}^{\infty} \left[\int_{-\infty}^{\infty} \mathfrak{F}_1\{g_\theta(R)\} \cdot |\rho| e^{i2\pi\rho R} \right] \delta(x \cos \theta + y \sin \theta - R) dR \quad (7.53)$$

$$= \int_0^{\pi} d\theta \int_{-\infty}^{\infty} \mathfrak{F}_1^{-1}[\mathfrak{F}_1\{g_\theta(R)\} \cdot |\rho|] \delta(x \cos \theta + y \sin \theta - R) dR. \quad (7.54)$$

Here it is clearly seen that the function back-projected at all angles is a filtered version of the projection $g_\theta(R)$, where the filter provides a $|\rho|$ weighting. As in any filtering operation in the frequency domain, we first Fourier transform, multiply by the filter function, and then inverse transform.

CONVOLUTION—BACK PROJECTION

The back-projected function in (7.54) can be rewritten as

$$\mathfrak{F}_1^{-1}[\mathfrak{F}_1\{g_\theta(R)\} \cdot |\rho|] = g_\theta(R) * \mathfrak{F}_1^{-1}\{|\rho|\} \quad (7.55)$$

using the convolution theorem of Fourier transforms. The spatial equivalent of filtering with $|\rho|$ is convolving with the inverse transform of $|\rho|$ [Horn, 1978; Tanaka, 1979; Scudder, 1978]. This introduces the convolution–back projection method of reconstruction, which is by far the most widely practiced. Instead of filtering each projection in the frequency domain, each projection $g_\theta(R)$ is convolved with a function $c(R)$ and then back-projected. Since the convolution function $c(R)$ is chosen to correct the $1/r$ blur, the reconstruction is exact as given by

$$f(x, y) = \int_0^{\pi} d\theta \int_{-\infty}^{\infty} [g_\theta(R) * c(R)] \delta(x \cos \theta + y \sin \theta - R) dR. \quad (7.56)$$

As indicated in (7.55), the convolution function is given by

$$c(R) = \mathfrak{F}^{-1}\{|\rho|\}. \quad (7.57)$$

Unfortunately, this transform is not defined since the function is not integrable. However, we can evaluate the transform in the limit as

$$c(R) = \mathfrak{F}^{-1}\left\{\lim_{\epsilon \to 0} |\rho| e^{-\epsilon|\rho|}\right\} \quad (7.58)$$

which is an integrable function. Evaluating the transform, we have

$$|\rho| e^{-\epsilon|\rho|} = \rho[e^{-\epsilon\rho} H(\rho) - e^{+\epsilon\rho} H(-\rho)] \quad (7.59)$$

where $H(\cdot)$ is the unit step function, which is unity for positive arguments and zero otherwise, as defined in Chapter 2. We first find the inverse transform of the bracketed portion as given by

$$\mathfrak{F}^{-1}\{[\cdot]\} = \int_0^{\infty} e^{-\epsilon\rho} e^{i2\pi R\rho} d\rho - \int_{-\infty}^{0} e^{\epsilon\rho} e^{i2\pi R\rho} d\rho$$

$$= \frac{i4\pi R}{\epsilon^2 + (2\pi R)^2}. \quad (7.60)$$

The completed inverse transform is evaluated using the relationship

$$\mathfrak{F}^{-1}\{\rho A(\rho)\} = \frac{1}{2\pi} a'(R). \quad (7.61)$$

Therefore,

$$\mathfrak{F}^{-1}\{|\rho| e^{-\epsilon|\rho|}\} = \mathfrak{F}^{-1}\{\rho[\cdot]\} = \frac{2(\epsilon^2 - 4\pi^2 R^2)}{(\epsilon^2 + 4\pi^2 R^2)^2}. \quad (7.62)$$

The convolution function $c(R)$ is therefore the limit of (7.62) as $\epsilon \to 0$.

The various properties of this convolution function can be put in a logical framework, keeping in mind the fact that the convolution function is the inverse transform of $|\rho|$. Using known theorems of Fourier transforms, we know that the average value of a function is equal to the value of its transform at the

origin. Thus, since $|\rho|$ is zero at the origin, we know that the average integrated value of $c(R)$ must be zero. This is the case for the function given by (7.62). Using this same relationship in reverse, we know that the value of $c(R)$ at the origin must approach the integrated average of $|\rho|$. The area of $|\rho|$ is equal to the limit, as $\rho \longrightarrow \infty$, of $\frac{1}{2}\rho^2$. This is in keeping with the value of $c(R)$ at the origin in the limit, as $\epsilon \longrightarrow 0$, of $2/\epsilon^2$.

Figure 7.12 illustrates a simplified sketch of the convolution function $c(R)$. In the vicinity of the origin, where $R^2 \ll \epsilon^2/4\pi^2$, the function is given by $2/\epsilon^2$. For higher values of R, where $R^2 \gg \epsilon^2/4\pi^2$, the function approaches $-1/2\pi^2R^2$, as shown in Fig. 7.12.

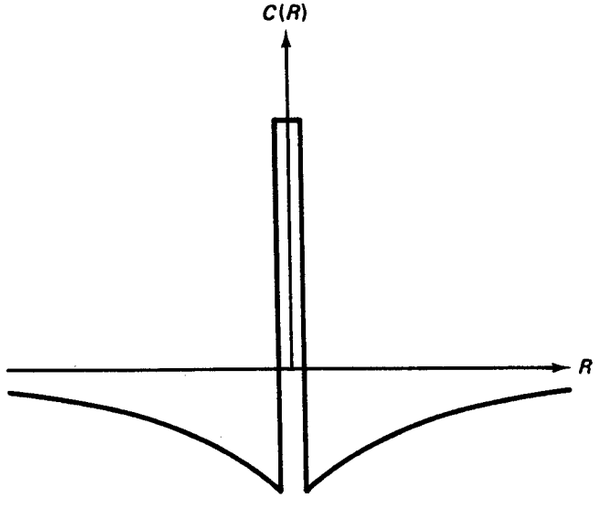

FIG. 7.12 Convolution function to undo $1/r$ blur.

It is interesting to note that the desired convolution function $c(R)$ could have been devised without using the central section theorem. We can make use of linear systems considerations in that any function $c(R)$ which results in the proper reconstruction of an impulse, without the $1/r$ blur, will accurately reconstruct all functions. For example, in equation (7.56), we require a $c(R)$ that will produce an impulsian $f(x, y)$ when $g_\theta(R) = \delta(R)$, the projection of an impulse at the origin. Essentially, this requires that $c(R)$, back-projected at all angles, will produce an impulsian reconstruction.

For the $c(R)$ in the limit given in (7.62), back-projecting at all angles provides the system impulse response as given by

$$h(r) = \int_0^\pi d\theta \int_{-\infty}^{\infty} c(R)\delta[r\cos(\theta - \phi) - R]dR$$

$$= \lim_{\epsilon \to 0} 2\int_0^\pi \frac{\epsilon^2 - 4\pi^2 r^2 \cos^2(\theta - \phi)}{[\epsilon^2 + 4\pi^2 r^2 \cos^2(\theta - \phi)]^2} d\theta. \tag{7.63}$$

Performing this complex integration, we arrive at the result

$$h(r) = \lim_{\epsilon \to 0} K\frac{\epsilon}{(\epsilon^2 + 4\pi r^2)^{3/2}} \tag{7.64}$$

where K is a constant. This is clearly an "impulsian" function having a value of K/ϵ^2 at the origin and zero elsewhere. Other forms of $c(R)$ in the limit provide similar results [Horn, 1978].

We now consider more realistic convolution functions which have well-behaved properties. For example, any physical system has an upper frequency limit imposed by either the geometry of the system, such as a finite beam size, or by electrical limitations such as noise. Thus the filtering imposed by the convolution filter could be of the form $|\rho|\,\mathrm{rect}\,(\rho/2\rho_0)$, where ρ_0 is the cutoff frequency. This filter is illustrated in Fig. 7.13.

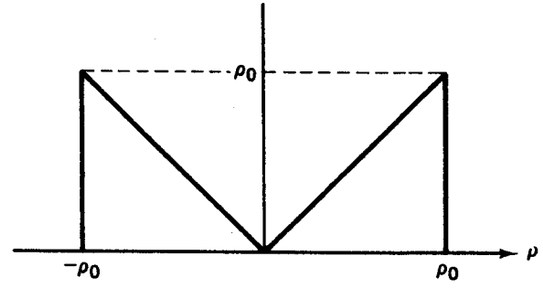

FIG. 7.13 Filtering function with band limiting.

To facilitate taking Fourier transforms, this function is modeled as

$$|\rho|\,\mathrm{rect}\left(\frac{\rho}{2\rho_0}\right) = \left[\mathrm{rect}\left(\frac{\rho}{2\rho_0}\right) - \Lambda\left(\frac{\rho}{\rho_0}\right)\right] \tag{7.65}$$

where the convolution function is given by

$$\mathfrak{F}^{-1}\left\{|\rho|\,\mathrm{rect}\left(\frac{\rho}{2\rho_0}\right)\right\} = \rho_0(2\,\mathrm{sinc}\,2\rho_0 R - \mathrm{sinc}^2\,\rho_0 R). \tag{7.66}$$

Thus a bandlimited function can be reconstructed by taking each projection $g_\theta(R)$, convolving with $\rho_0(2\,\mathrm{sinc}\,2\rho_0 R - \mathrm{sinc}^2\,\rho_0 R)$, and back projecting. If we take the limit of this bandlimited function as $\rho_0 \longrightarrow \infty$, we get an expression similar to that of (7.62).

In practice, a wide variety of convolution functions are used which are similar to that of (7.65). The convolution kernel $c(R)$ is a convenient place to accomplish the overall system filtering in addition to the basic $|\rho|$ filtering. In general, as with most imaging systems, these filters are a compromise between signal-to-noise ratio and resolution. Thus these filters generally involve the product of $|\rho|$ and some high-frequency cutoff filter. Since the sharp cutoff of a rect function generally causes "ringing" at edges, gentler rolloff characteristics are usually used.

RECONSTRUCTION OF THE ATTENUATION COEFFICIENT

The reconstruction methods studied indicated how a two-dimensional function could be reconstructed from its line integrals. These line integrals are the sum of the function in different directions. In the case of x-ray attenuation, however, we measure the exponent of the desired line integral as given by

$$I = I_0 e^{-\int \mu(z) dz} \tag{7.67}$$

where, for convenience, we consider a single ray in the z direction. Note that we have a nonlinear relationship between the measured projection and the desired line integral. This non linearity can be removed if we use, as our measured data, the log of the measured transmission where

$$\ln\left(\frac{I_0}{I}\right) = \int \mu(z)\, dz. \tag{7.68}$$

In x-ray attenuation considerations, the logarithm of the measured intensity at many positions and angles is used with one of the reconstruction methods previously described to form a cross-sectional image of the linear attenuation coefficients.

The removal of the nonlinearity has within it a number of inherent assumptions, namely, that the source is monoenergetic and that the beam is infinitesimally narrow. Unfortunately, both of these assumptions lead to relatively impractical systems as far as getting sufficient photon flux to obtain a statistically meaningful measurement. Thus, to provide a source of adequate strength, a polychromatic source is used providing a measured transmission given by

$$I = \int S(\mathcal{E}) \exp\left[-\int \mu(z, \mathcal{E}) dz\right] d\mathcal{E} \tag{7.69}$$

where $S(\mathcal{E})$ is the source spectrum. In this case the line integral is not directly measured and the resultant behavior is nonlinear [Stonestrom et al., 1981]. Here we attempt to reconstruct $\mu(\bar{\mathcal{E}})$, where $\bar{\mathcal{E}}$ is the average energy emerging from the object. Taking logs as in (7.68), we obtain

$$\ln\left(\frac{I_0}{I}\right) = a_0 + a_1 \int \mu(z, \bar{\mathcal{E}})\, dz + a_2\left[\int \mu(z, \bar{\mathcal{E}}) dz\right]^2 + \dots \tag{7.70}$$

where $I_0 = \int S(\mathcal{E}) d(\mathcal{E})$, the total source energy. We have a distorted version of the desired line integral.

The nature of the distortion can be seen by studying a single pixel in a cross section traversed by a number of rays at different angles. Along each ray we are attempting to measure the line integral or the sum of the attenuation coefficients of each pixel. The attenuation coefficient of the single pixel being studied should contribute a given μ to each sum. However, each ray can contain different materials providing different degrees of spectral shift and a resultant different average energy $\bar{\mathcal{E}}$. Thus the single pixel has different contributions to each ray sum, resulting in a distortion in the attempted reconstruction. From this discussion it is seen that the largest distortions will occur in the vicinity of bone where the greatest spectral shifts occur. In early head scans this effect resulted in a severely cusped region immediately inside the skull, making diagnosis of this region very difficult.

These nonlinear terms cause distortions in the reconstructed image which can be quite severe. As a result, most instruments use a nonlinear function of the log of the measurements in an attempt to compensate for the nonlinearity. Unfortunately, the degree of nonlinearity depends on the materials in the path, which are not known beforehand. This problem has been minimized in some computerized tomography scanners by using a water bag around the region being scanned, thus providing a constant known path length. This approach still provides some error since the amount of bone and air within each path is still unknown. Other approaches are under investigation. In one, an initial reconstruction is provided which includes the distortions or spectral shift artifacts. From this initial reconstruction the amount of bone and soft tissue in each path can be estimated and used to provide a more accurate nonlinear correction.

The other nonlinearity is that due to finite beam size. The projection for a finite beam size is given by

$$I = \iint s(x, y) \exp\left[-\int \mu(x, y, z) dz\right] dx dy \tag{7.71}$$

where $s(x, y)$ is the source intensity as a function of its lateral dimensions. For clarity we assume a monoenergetic beam in this case. As before, the error with this system depends on the variation in $\mu(x, y)$ over the beam size $s(x, y)$. If, over the beam region, $\mu(x, y)$ is relatively constant at some value $\bar{\mu}$, the measurement can be approximated as

$$\ln\left(\frac{I_0}{I}\right) \simeq \int \bar{\mu}(z) dz \tag{7.72}$$

where

$$I_0 = \iint s(x, y) dx dy.$$

Unfortunately, there are many discontinuities in the attenuation coefficient, such as the edges of bone, so that this approximation is often inaccurate. This remains a source of error in existing instruments which is minimized through the use of relatively narrow beams.

SCANNING MODALITIES

In Fig. 7.4 we illustrated a simple method of data acquisition where a single source and detector are synchronously scanned to provide the required projection data. This system, because of chronology, is known as a "first-generation"

scanner. It is identified by a two-motion translate–rotate scan using a single detector. The principal difficulty with this instrument is its relatively long scan time, on the order of a few minutes. Only a small portion of the total x-ray output of the x-ray tube is utilized, requiring relatively long scanning times to achieve adequate statistics. These long times are acceptable, however, for relatively stationary regions such as the head. These scanners continue to achieve relatively wide use because of their low cost. However, even as a head scanner, there are continuing problems with uncooperative patients such as children and patients with poor motor control.

Figure 7.14 is an illustration of a second-generation scanner at various intervals of the scan. Here the same translate–rotate motions are used with a multiple-detector system. In this way, several projections are acquired during each traverse. For example, if there are 10 detectors, each 1° apart, a single translation acquires all 10 projections. During the subsequent rotation the gantry is indexed 10° rather than 1°, resulting in a 10: 1 time reduction. Since 10 times as much of the x-ray output is being utilized, the scan time is cut accordingly. Using this approach, scan times have been reduced to a fraction of a minute.

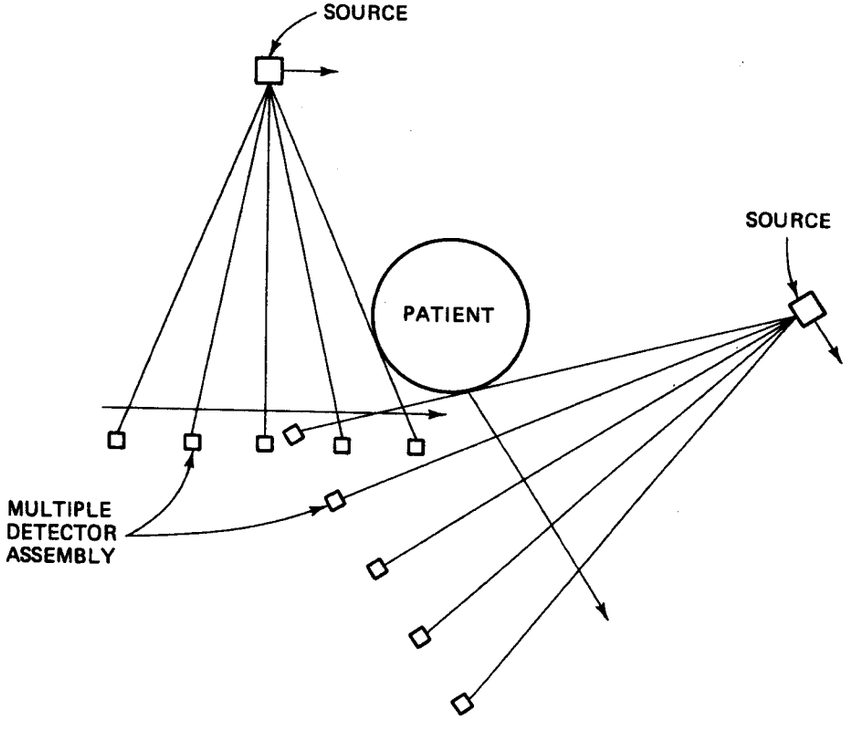

FIG. 7.14 Second-generation scanner, using multiple detector translate-rotate system.

One important feature of both first- and second-generation scanners is self-calibration. Either preceding or following each traverse, each x-ray beam impinges on the detector with no intervening material. This provides a reference measurement of I_0, the intensity in the absence of attenuation. This value is required to calculate the line integral. Although it is theoretically constant, drifts in both source and detector often require frequent measurements.

The third-generation scanner involves rotation-only of a fan beam, as illustrated in Fig. 7.15. Both the source and the detector are rotated about a common center within the patient. The detector array is a few hundred contiguous elements. The primary advantage of this approach is the mechanical simplicity and associated ability to provide very high speeds, with scan times as low as 1 sec. The detectors can be relatively deep and positioned along the rays radiating from the source. This relatively long path length has enabled the use of gaseous ionization detectors using xenon.

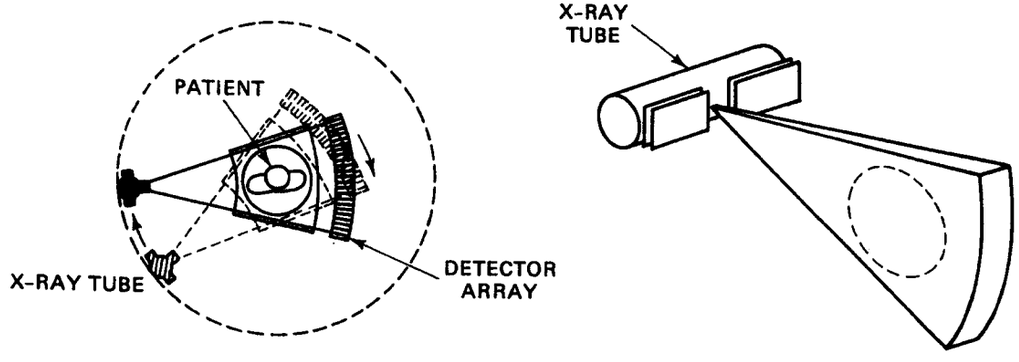

FIG. 7.15 Third-generation fan-beam scanner, using a rotating source and detector array. (Courtesy of the General Electric Medical Systems Division.)

One disadvantage of this system is the lack of self-calibration. At no point after the patient enters the machine can the system be calibrated. In the earlier days of these instruments "ring artifacts" were prevalent due to errors in individual detectors which were uncalibrated. These have since been minimized through improved detectors and software corrections. A commercial third-generation system is illustrated in Fig. 7.16.

The fourth-generation scanner is characterized by a rotating fan beam impinging on a 360° stationary detector array as illustrated in Fig. 7.17. A source, generating a fan beam, is rotated around the patient. The transmitted rays are collected by the stationary detector array. This simple mechanical motion of the source only allows for a rapid scan time. In addition, the system is again self-calibrating since, at different portions of the scan, each detector is irradiated by the source without any intervening material. Also, the system is relatively

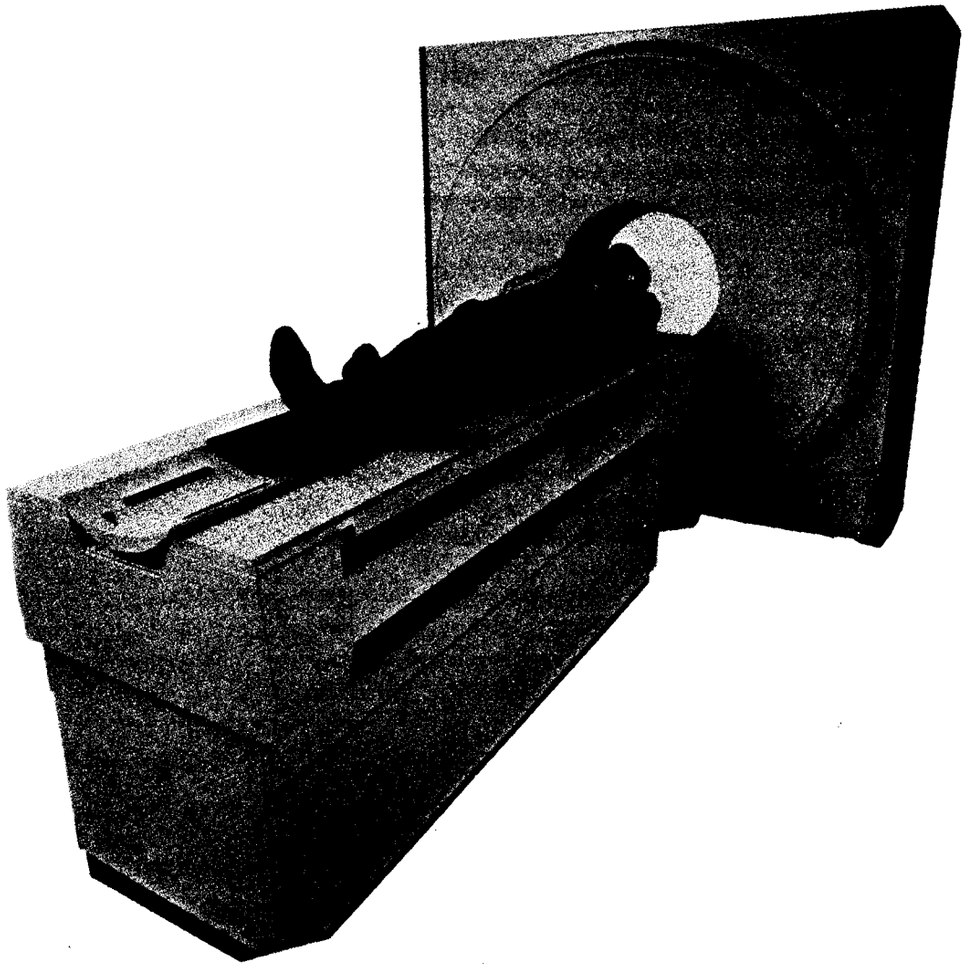

FIG. 7.16 Third-generation commercial scanner. (Courtesy of the General Electric Medical Systems Division.)

immune to ring artifacts since detector errors are distributed throughout the image, rather than representing a specific radius.

One difficulty with the scanner is the varying angle at which the rays strike the detectors. In the third-generation scanner the detectors could be aligned along the rays since the entire structure rotated. Here, however, at different source positions the rays strike a given detector at different angles. This means that the detectors should be relatively shallow to avoid the rays entering adjacent detectors. To provide high quantum efficiency with these shallow detectors, high-μ materials are used such as scintillators with high atomic numbers. Gaseous detectors, having lower linear attenuation coefficients, are not used with stationary detector systems.

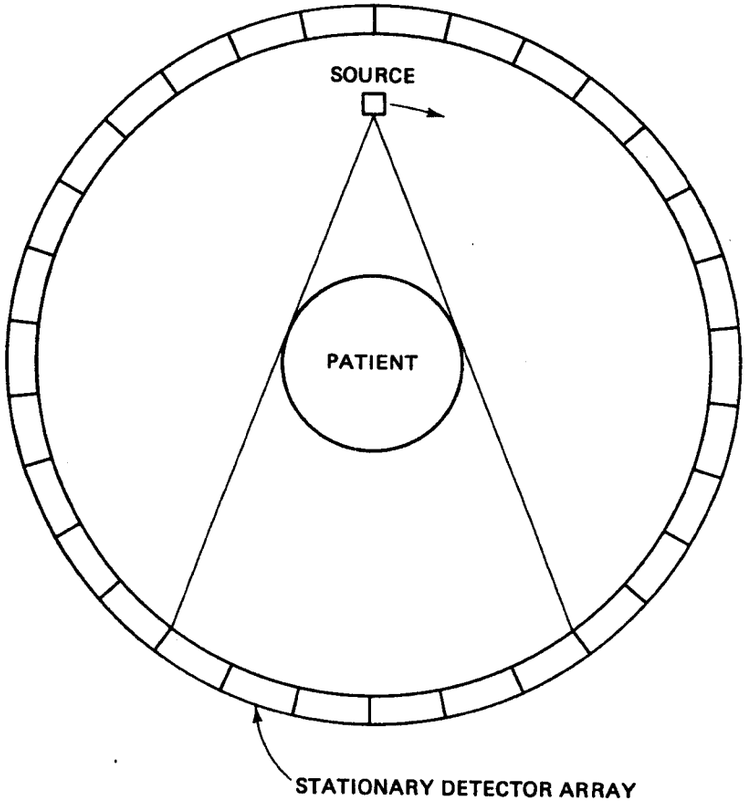

FIG. 7.17 Fourth-generation scanner, using a rotating fan-beam and a stationary ring detector array.

The third- and fourth-generation scanners derive their measurements using fan-beam rather than parallel-beam projections. These require somewhat modified approaches to the reconstruction problem. One approach is known as re-binning, where the various fan-beam rays from different projections are reassembled as parallel-beam projections. These then require the same reconstruction algorithms as the first- and second-generation scanners. An alternative approach is the use of a modified convolution back-projection system [Gullberg, 1979; Denton et al., 1979]. Here the convolution kernel is slightly different and the back projection involves a quadratic weighting factor rather than the uniform weighting of the parallel rays. This latter algorithm is widely used in existing scanners.

The image quality of these systems has improved significantly in recent years, as has their diagnostic value. Typical head and body images made with a third-generation scanner are illustrated in Figs. 7.18 and 7.19.

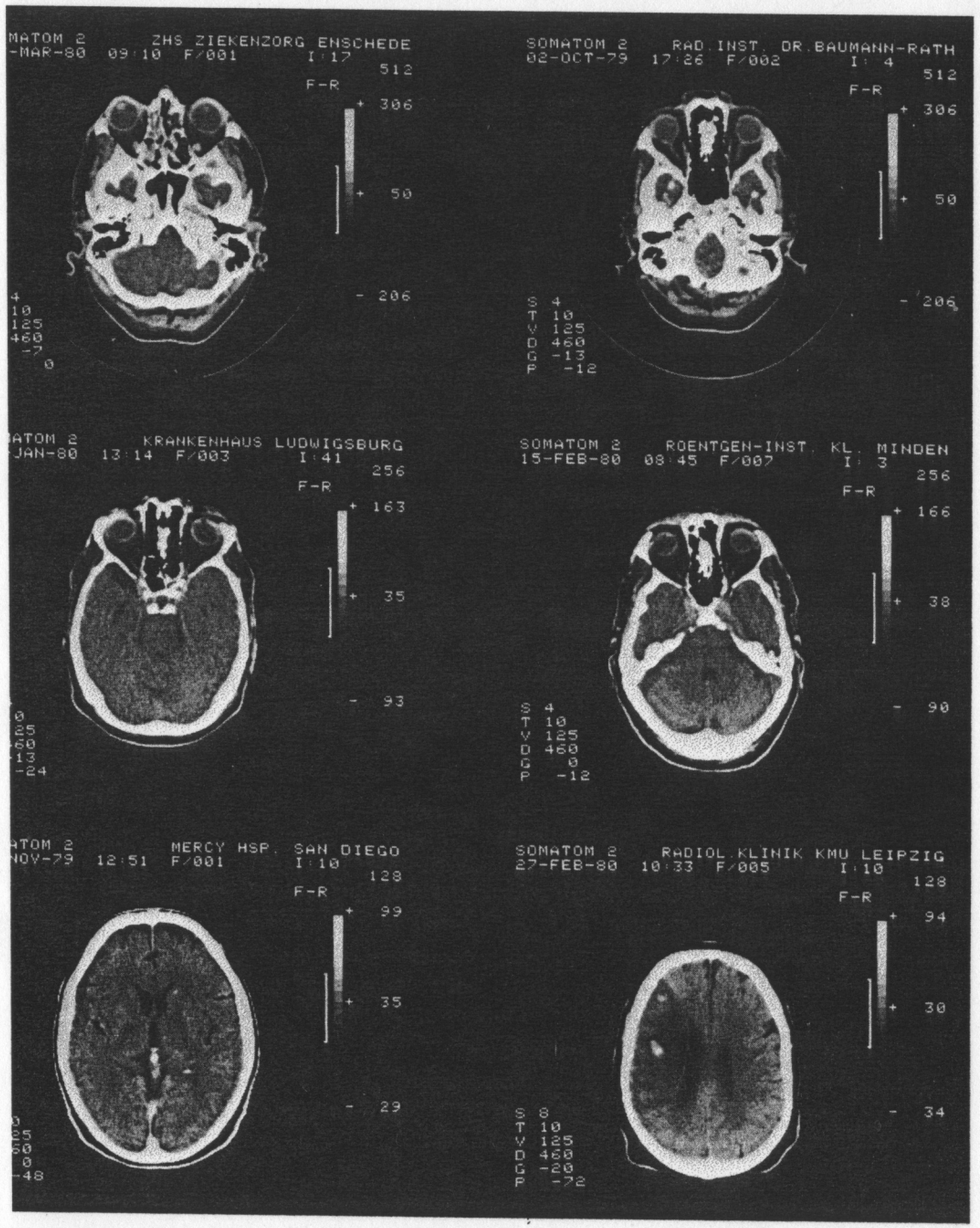

FIG. 7.18 Cross-sectional head images at different levels, made with a third-generation scanner. (Courtesy of the Siemens AG-Bereich Medizinische Technik.)

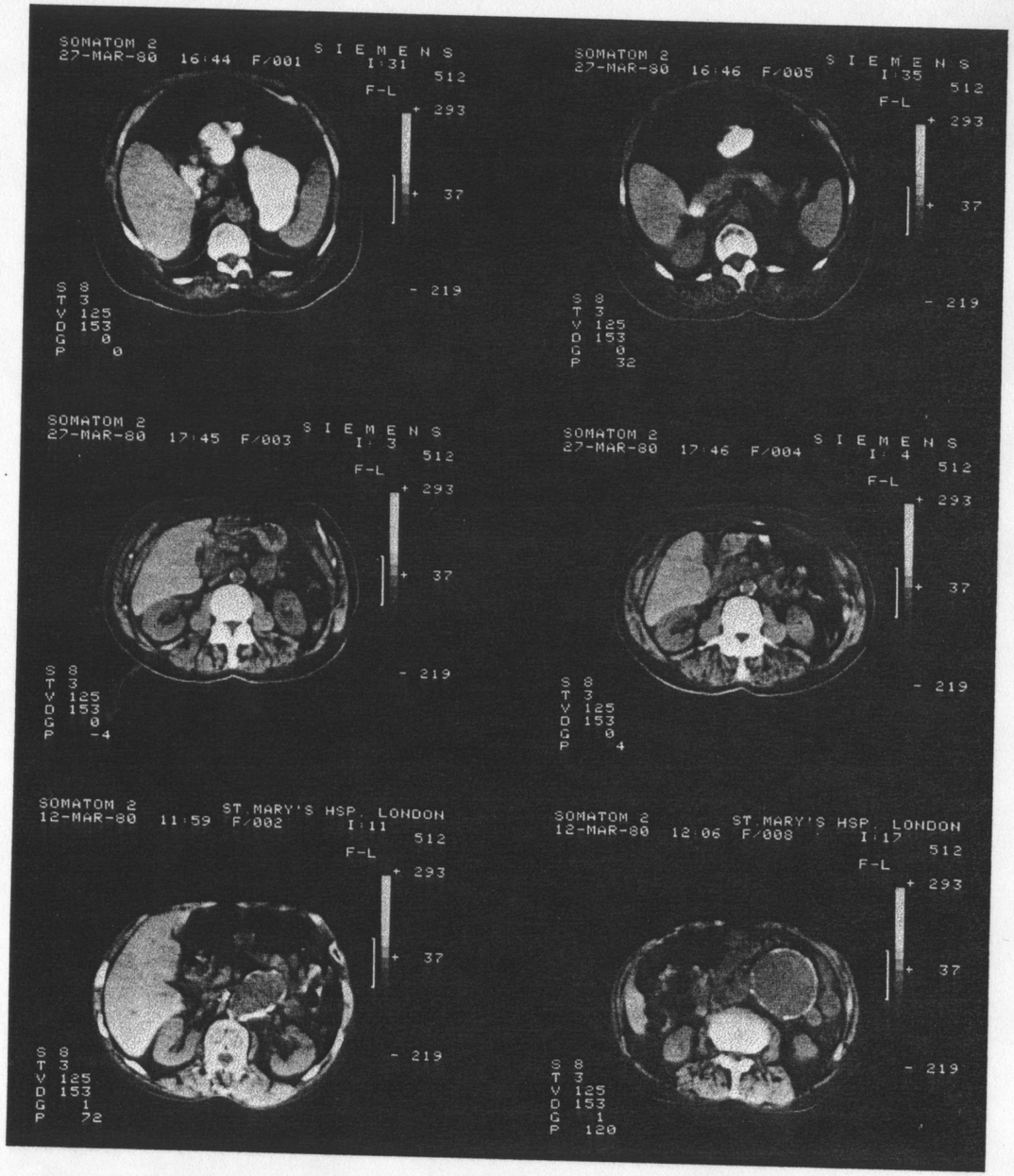

FIG. 7.19 Cross-sectional body images at different levels, made with a third-generation scanner. (Courtesy of the Siemens AG-Bereich Medizinische Technik.)

NOISE CONSIDERATIONS IN COMPUTERIZED TOMOGRAPHY

The noise considerations of the measurements in computerized tomography are similar to those of projection radiography [Chesler et al., 1977; Brooks and DiChiro, 1976a]. We have an array of independent measurements, each having the general form

$$N_i = n_0 \mathrm{A} \exp\left(-\int_i \mu dl\right) \tag{7.73}$$

where N_i is the number of detected photons at each measurement, n_0 is the incoming photon density in photons per unit area, A is the active area of the detector receiving the impinging x-ray beam, and $\int_i \mu dl$ is the ith line integral of the cross section $\mu(x, y)$, representing one of the rays. For simplicity, the collection efficiency η is assumed to be unity, a reasonable assumption with available detectors used in CT. As in projection radiography, the noise or standard deviation of each measurement is $\sqrt{N_i}$ because of the Poisson statistics.

In computerized tomography, however, we first calculate the line integrals of μ using logs and then, using the line integrals, reconstruct the values of μ. The line integrals are given by

$$g_i = \int_i \mu dl = \ln\left(\frac{N_0}{N_i}\right) \tag{7.74}$$

where $N_0 = n_0 A$, the incident number of photons per measurement. Using this relationship, we calculate the mean $\bar{g}_i$ and σ_{g_i}, the standard deviation of the line integral resulting from the uncertainty in the measurement of N_i.

The mean and variance of the line integral of the projection have been derived in Chapter 6. For a reasonably large number of photons per measurement N_i, the mean and variance of the line integral are given by

$$\bar{g}_i \simeq \ln\left(\frac{N_0}{\bar{N}_i}\right) \tag{7.75}$$

$$\sigma_{g_i}^2 \simeq \frac{1}{\bar{N}_i} \tag{7.76}$$

where $\bar{N}_i$ is the mean of the number of counts per measurement.

Using these statistics of the line integral measurement of the reconstructed image $\mu(x, y)$, we wish to analyze the signal-to-noise ratio as given by

$$\mathrm{SNR} = \frac{C\bar{\mu}}{\sigma_\mu} \tag{7.77}$$

where C, as with projection systems, is the fractional change in μ, $\bar{\mu}$ is the mean, and σ_μ is the standard deviation. We now proceed to calculate $\bar{\mu}$ and σ_μ for a set of discrete projections in an appropriately normalized fashion. For convenience

we introduce the notation $R' = r\cos(\theta - \phi)$ so that the back-projection operator takes the form $\delta(R - R')$.

Using the convolution–back projection system, the resultant reconstruction is given by

$$\mu(x, y) = \int_0^\pi [g_\theta(R') * c(R')]d\theta \tag{7.78}$$

where $g_\theta(R)$ represents the projection at the angle θ, $c(R)$ is the convolution function, and each has been convolved with $\delta(R - R')$, the back-projection operator. For studying noise we use a realistic model of M discrete projections as given by

$$\hat{\mu} = \sum_{i=1}^{M} [g_{\theta_i}(R') * c(R')]\Delta\theta \tag{7.79}$$

where $\hat{\mu}$ is the estimate of μ. To evaluate the required normalization and facilitate the use of transforms, we express this finite sum in integral form as

$$\hat{\mu} = \frac{M}{\pi}\int_0^\pi [g_\theta(R') * c(R')]d\theta \tag{7.80}$$

where $\Delta\theta = \pi/M$. This can be expressed as a two-dimensional convolution of the desired function $\mu(r, \phi)$ as

$$\hat{\mu} = h(r, \phi) ** \mu(r, \phi) \tag{7.81}$$

where $h(r, \phi)$ is the two-dimensional impulse response as given by

$$h(r, \phi) = \frac{M}{\pi}\int_0^\pi c[r\cos(\theta - \phi)]d\theta. \tag{7.82}$$

For this analysis it is convenient to normalize the area of $h(r, \phi)$ to unity so that the reproduced values of $\hat{\mu}$, in broad constant areas, will not be scaled and will represent the correct average value. We thus require that

$$\int_0^{2\pi}\int_0^\infty h(r, \phi) r dr d\phi = 1. \tag{7.83}$$

The impulse response having a unity area is equivalent to its Fourier transform $H(\rho)$ being unity at the origin.

Taking transforms using equation (7.82), we obtain

$$H(\rho) = \frac{M}{\pi}\frac{C(\rho)}{|\rho|} \tag{7.84}$$

where $H(\rho)$ is the transform of the circularly symmetric impulse response and $C(\rho)$ is the Fourier transform of the convolution function $c(R)$. Division by $|\rho|$ is again the affect of back projection. $C(\rho)$ can be decomposed as given by

$$C(\rho) = |\rho| S(\rho) \tag{7.85}$$

where $|\rho|$ removes the back-projection blur and $S(\rho)$ is the system filter. Thus

the normalization procedure requires that

$$S(0) = \frac{\pi}{M}.$$

For example, using the rectangular filter of Fig. 7.13, we obtain

$$C(\rho) = |\rho| \frac{\pi}{M} \operatorname{rect}\left(\frac{\rho}{2\rho_0}\right). \tag{7.86}$$

We will calculate the signal-to-noise ratio using this filter function.

In taking the variance of the estimate of μ we use the statistical property that the variance of a sum of independent measurements is equal to the sum of the variances. For a weighted sum of measurements, the weightings are squared in accordance with the definition of the variance in (2.49). Since each measurement is weighted by $c(R)$, the resultant measurement variance is weighted by $[c(R)]^2$. The variance of the reconstruction is therefore the variance of the measurements convolved with $[c(R)]^2$ and back-projected. In integral form this is given by

$$\sigma_\mu^2 = \frac{M}{\pi} \int_0^\pi \sigma_{g_\theta}^2(R') * [c(R')]^2 d\theta \tag{7.87}$$

where $\sigma_{g_\theta}^2(R)$ is the variance of g_θ along each projection. In the continuous case, from (7.76), it is given by

$$\sigma_{g_\theta}^2(R) = \frac{1}{\bar{n}_\theta(R)h} \tag{7.88}$$

where $\bar{n}_\theta(R)$ is the average transmitted photon density and h is the height of the beam normal to the section. The $\bar{n}h$ represents the number of transmitted photons per unit distance along the projection.

To achieve useful results, we assume a typical radiographic object where the density of transmitted photons $\bar{n}_\theta(R)$ is relatively constant and can be approximated by a constant $\bar{n}$. In that case the convolution becomes an integral of $c^2(R)$ and the variance becomes

$$\sigma_\mu^2 = \frac{M}{\pi} \frac{1}{\bar{n}h} \int_0^\pi d\theta \int_{-\infty}^{\infty} c^2(R) dR = \frac{M}{\bar{n}h} \int_{-\infty}^{\infty} c^2(R) dR. \tag{7.89}$$

We evaluate this integral using Parseval's theorem, giving

$$\sigma_\mu^2 = \frac{M}{\bar{n}h} \int_{-\infty}^{\infty} |C(\rho)|^2 d\rho. \tag{7.90}$$

Using the normalized rectangular filter from (7.86), we obtain

$$\sigma_\mu^2 = \frac{M}{\bar{n}h} \int_{-\infty}^{\infty} \rho^2 \frac{\pi^2}{M^2} \operatorname{rect}\left(\frac{\rho}{2\rho_0}\right) d\rho = \frac{\pi^2}{\bar{n}hM} \frac{2\rho_0^3}{3}. \tag{7.91}$$

The resultant signal-to-noise ratio is therefore

$$\text{SNR} = \frac{C\bar{\mu}}{\sigma_\mu} = \frac{C\bar{\mu}\sqrt{\frac{3}{2}\bar{n}hM}}{\pi} \rho_0^{-3/2}. \tag{7.92}$$

It is more useful to structure the result, as before, in terms of resolution limitations imposed by the detector width w so that the trade-off between resolution and signal-to-noise ratio is readily visualized. Obviously, increasing the bandwidth ρ_0 without bound would be poor design since the signal-to-noise ratio would become poorer while the resolution would continue to be limited by the effective detector width w. Thus, in a good design, the bandwidth ρ_0 is compatible with a resolution equal to the detector width. Thus we have

$$\rho_0 = \frac{K}{w} \tag{7.93}$$

where K is a constant of order unity depending on the shape of the system response. This constant will vary slightly depending on which resolution criteria is used. The signal-to-noise ratio then becomes

$$\text{SNR} = K' C\bar{\mu}\sqrt{\bar{n}hM}\, w^{3/2} \tag{7.94}$$

where K' is a combined constant, again of order unity.

It is indeed interesting to study the implications of the resultant signal-to-noise ratio. Considerable insight can be derived by structuring this relationship in terms of $\bar{N}$, the average number of counts per measurement as given by

$$\text{SNR} = K' C\bar{\mu}\sqrt{\bar{N}M}\, w \tag{7.95}$$

where $\bar{N} = \bar{n}A = \bar{n}wh$.

In our noise studies in projection radiography in Chapter 6, the signal-to-noise ratio was shown to be dependent solely on the number of counts per measurement. The counts per measurement were governed by the imput radiation, the body attenuation, and the area of a pixel. Here we see the additional factor w. Thus, in computerized tomography, a higher-resolution system suffers an additional noise penalty, over and above the reduced number of photons per element for a given dose. This increased penalty is a result of the convolution operation, which couples the noise values of adjacent measurements into each measurement. The procedure that decouples the signal information, removing the $1/r$ blur, increases the noise since the signal is subjected to a $c(R)$ convolution while the noise variance experiences a $c^2(R)$ convolution as indicated in (7.87).

The analysis using a continuous measured projection $g_\theta(R)$ ignored the finite width of the detector w. Effectively, for a simple single scanned detector system as shown in Fig. 7.4, the projection is being convolved with a detector or beamwidth function such as rect (R/w). This can be treated as part of the overall convolution function $c(R)$. Thus $c(R)$ becomes the convoution of rect (R/w) and the function used for reconstruction. For detector arrays this situation becomes more complex because of the aliasing, which is introduced when $g_\theta(R)$ is sampled.

PROBLEMS

7.1 In a linear tomography system a source a distance d from the film is moved uniformly an amount X in the x direction with the film moved an amount kX in the opposite direction. A sinusoidal transparency having a transmission

$$t = a + b \cos 2\pi f_0 x$$

is imaged. At what depths z will the sinusoidal component at f_0 disappear?

7.2 In an x-ray imaging system the desired information is at plane $z = d/2$ and the undesired structure, at plane $z = 2d/3$, consists of a symmetrical square wave in the x direction of period W.
(a) Find the parameters k and X of a linear motion tomography system that will focus on the desired plane and eliminate the square-wave structures.
(b) At what other depth planes will this square-wave grating disappear?

7.3 An x-ray source, parallel to and a distance d from the x-ray recorder, has a pattern in the x direction of rect (x_0/X). It is moved linearly in the x direction an amount D with the recorder moved in the opposite direction an amount kD where $D > X$.
(a) Find the two z distances for placing a transparency at which the point-spread function due to the source alone is equal to that due to the motion alone.
(b) Plot the point response at the recorder, in the x direction, for these two z planes labeling the break points.
(c) Plot the point response for planes at $z = d$, $z = d/(1 + k)$, $z = d/(1 + k/2)$.

7.4 In a linear tomography system a source is moved a distance A in the x direction with the recorder moved kA in the opposite direction. The source distribution in the x direction is rect (x/X), a distance d from the recorder.
(a) At what two depth planes is the response a rect function? What are the widths?
(b) At what two planes is the response a triangular function, and what is the width of the response at each plane?

7.5 In a linear tomography system the source is translated in the x direction at a velocity v for a time interval τ. The recorder is linearly translated in the opposite direction with a velocity kv for the same time interval. The source distribution in the x direction is given by rect (x/X).
(a) Find the overall point response in the x direction as a function of z.
(b) Find the thickness of the tomographic cut, which is defined as the distance between those z planes where the size of the response due to the source motion alone is equal to the response size due to the source alone.

7.6 An x-ray imaging system consists of a circular disk source of radius r_s separated a distance d from a film–screen system which has an impulse response circ (r/r_f). The source is linearly translated in the x direction an amount A with the film moved kA in the opposite direction.
(a) Find the impulse response of the system for a transparency at plane z.
(b) A transparency consists of two pinholes separated in the x direction by S. Over what depth range can the transparency be placed with the resultant images separated, that is, not overlapping?
(c) Repeat part (b) for two holes of radius r_h.

Make the necessary assumptions concerning the relative dimensions such that the images are separable in the absence of translation.

7.7 (a) Find the projection space $g(R, \theta)$ of a two-dimensional function $f(x, y) = \cos 2\pi f_0 x$. Using the filtered back-projection reconstruction system, find the back-projected function. Show that this function results in a correct reconstruction.
(b) Repeat part (a) for $f(x, y) = \cos 2\pi ax + \cos 2\pi by$ and $f(x, y) = \cos 2\pi(ax + by)$.

7.8 Find the circularly symmetric function $f(r)$ which has a projection at all angles of

$$p(R) = \sqrt{1 - R^2}\ \text{rect}\,\frac{R}{2}.$$

[*Hint:* Use Fourier transform tables in Bracewell (1965).]

7.9 The area of a two-dimensional function is $\iint f(x, y)dxdy$.
(a) Find an expression for the area in terms of the projection $g_\theta(R)$.
(b) Show that the function $h_R(R)h_\theta(\theta)$ cannot represent a projection $g(r, \theta)$ unless $h_\theta(\theta)$ is a constant.

7.10 In a computerized tomography system each projection is obtained using a uniform scanning beam of width W instead of an infinitesimal pencil beam. Find the resultant estimate $\hat{f}(x, y)$ of the function $f(x, y)$ using a conventional reconstruction system that does not take the beam width into account.

7.11 Find the signal-to-noise ratio of the computerized tomography reconstruction of a lesion immersed in a 20-cm cylinder of water whose attenuation coefficient is 5% different than that of the water. A scanned source is used providing 100 projections at 0.1R per projection. The detector and beam dimensions are 2.0 × 2.0 mm. Make appropriate assumptions about the reconstruction filter.

7.12 Projections $g_\theta(R)$ are taken of a unit square where $f(x, y) = \text{rect}\,(x)\,\text{rect}\,(y)$.

(a) Find a general expression for $g_\theta(R)$ and the particular functions for $\theta = 0°$ and $45°$.

(b) Using the method of filtered back projection, find the *Fourier transform* of the back-projected function for the general case and for $\theta = 0°$ and $45°$.

7.13 In the convolution back projection reconstruction system, find a general expression for the impulse response of the reconstruction $h(r)$ for a convolution function $c(R)$. The answer can be left in integral form and should be a function of r and R only.

8

Nuclear Medicine

In radiography the regions under study are used in a transmission mode in the measurement of the attenuation coefficient. This measurement is often enhanced by the selective administration of radiopaque contrast materials. In nuclear medicine [Blahd, 1965] the region under study becomes an active source. This is done through the selective administration of radioactive materials since the body contains no natural radioactive substances. Either the radioactive material itself, or the chemical form it is bound in, has properties that cause it to be selectively taken up in specific regions of the anatomy. Once taken up in the organs of interest, these become radiating sources. Thus the imaging problem in nuclear medicine is that of defining a three-dimensional source distribution rather than a distribution of attenuation coefficients.

It is important to point out that, in general, much smaller amounts of administered materials are required in nuclear medicine than in radiographic contrast studies. The radiation dose problems are also quite different. In radiography the patient is irradiated only during the time the x-ray beam is turned on. In nuclear medicine the patient is being irradiated from the moment the radioactive material is administered until it is either eliminated by the body or decays.

The earliest nuclear medicine studies were made on the thyroid gland by taking advantage of its natural affinity for iodine. An isotope of iodine ^{131}I was used as the tracer material. This emits gamma rays at an energy of 364 kev.